Environment-Aware Localization for Wireless Sensor Networks using Magnetic Induction

Xin Tan, Zhi Sun, Pu Wang, and Yanjing Sun

Abstract—The Magnetic Induction (MI) communication techniques can enable or enhance many wireless applications in the complex environments where line-of-sight (LOS) links do not exist. The critical position information of each wireless device can also be derived by the same MI systems without additional hardware or infrastructure. However, while MI signals can penetrate most of the transmission media without significant attenuation or phase shifting, the obstacles with high conductivity can still influence the signal propagation, which incurs additional positioning errors in the MI-based localization. To address such challenge, this paper develops an environment-aware MIbased localization technique for wireless sensor networks in complex environments with significant amount of high-conductive obstructions. First, the system architecture of the MI-based environment-aware localization and the MI channel is introduced. The environment-aware capability is realized by analyzing the unique MI response information gathered by each MI-based sensor node. Then, a joint device localization and environment sensing algorithm is developed to estimated the position of each device in the network as well as the distribution of the highconductive objects. Finally, the performance of the proposed solution is validated through both computer simulations and realworld experiments.

Index Terms—wireless sensor network, magnetic induction, localization, environment-aware.

I. Introduction

Due to the lack of the line of sight to satellites, the GPS, which is widely used to obtain the position information in outdoor environments cannot work in many places such as underground tunnels [2], [3], underwater environments [4] and indoor environments [5], [6]. The localization based on wireless sensor networks (WSN) becomes one of key technologies to address the challenges in these scenarios [7], [8], [9], [10]. Based on the signal strength or phase of the received signal obtained by the communications in the network, the internode distance can be estimated and then the position of each node can be determined by geometric calculations [11], [12], [13].

Numerous technologies including received signal strength indication (RSSI)[13], [14], [15], time of arrival (TOA) [16], and angle of arrival (AOA) [12], [17] can be utilized for the localization of WSNs. By capturing the information from the internode communications, such as signal strengths and

Xin Tan and Zhi Sun are with Department of Electrical Engineering, University at Buffalo, State University of New York, Buffalo, NY 14260, USA. E-mail: {xtan3, zhisun}@buffalo.edu. Pu Wang is with Department of Computer Science, University of North Carolina at Charlotte, Charlotte, NC 28223, USA. E-mail: Pu.Wang@uncc.edu. Yanjing Sun is with School of Information and Control Engineering, China University of Mining Technology, Xuzhou, Jiangsu, 221116, China. E-mail: yjsun@cumt.edu.cn. Zhi Sun handles the correspondence of this paper.

A much shorter preliminary version of this paper appeared in [1].

phases, the internode distances or orientations can be estimated by relating them with the channel model of the signal propagation. The positions of the sensor nodes are then estimated based on their relative positions. However, the problems exist when we apply these technologies in the complex environments. First, traditionally the localization technologies for the WSN are based on the EM signals received in the sensor nodes. Due to the rapid attenuation of the EM signal strength in the RF-challenging environments, such as underground and underwater environments, the sensor nodes can only be localized in very limited distance [18]. Second, existing localization techniques for WSNs are mainly based on deploying anchor nodes or RFID tags at predesigned positions, which requires pre-installed infrastructures in the environments [11], [19], [20], [21]. However, the pre-installed infrastructures are not feasible in many applications, such as the military or law enforcement missions in indoor environments and the exploration tasks in underground or underwater environments. Moreover, since the complex environments, such as indoor and in-pipe environments, usually consist of reflectors like walls, pipes, and rebar structures, error increases as the distance from the anchors or tags increases due to the severe propagation conditions of the radio channel influenced by the signal reflections. To address the problems caused by signal reflections and improve the localization accuracy, fingerprint database for localization is built by aforehand training measurements to better relate the signal strength with the device position [22], [23]. However, such strategies are based on aforehand experimental measurements and not applicable for unknown or dynamic environments.

To address the problems of the signal attenuation in RFchallenging environments, the magnetic induction (MI)-based communication has been proposed [24], [25], [26], [27], [28]. As shown in Fig. 1, the MI communication uses a small loop to generate magnetic field in high frequency (HF) band and receive the signal by capturing the induced current in another coil. Instead of using propagating EM waves, MI technique utilizes the near field of low frequency electromagnetic field to realize the wireless communication. Hence, it is not significantly influenced by the complicated underground or underwater medium because the magnetic permeability of in these medium is almost the same as that in air. Moreover, the MI channel is also reliable and determined since the MI signals are not easily reflected or scattered by the random obstructions. As a byproduct of the wireless communications, the same MI system can readily provide localization capability without any additional hardware or cost.

Although MI-based communication has more tractable

channels, it is still influenced by high-conductive objects in the complex environments. For example, if the MI coils are located near large metallic facilities, such as reinforcing bars, metallic pipes, and metallic walls, the magnetic field can not penetrate them. Eddy currents will be generated on these objects and they will excite new magnetic field to affect the primary field. Therefore, the influence from those highconductive objects need to be considered when we apply the MI-based localization in such complex environments. However, since the MI coils are sensitive to those highconductive objects nearby, it is possible to use the MI coil as a "radar" to detect and estimate those high-conductive objects. The magnetic field generated by the eddy currents on those objects will also be detected by the MI coil itself. By capturing the feedback by the MI coils, the distribution of the high-conductive objects can be estimated and it can be used as the environment-aware information to develop localization algorithms.

In this paper, an environment-aware localization strategy is developed for MI-based wireless networks in complex environments with arbitrary number of conductive objects. Specifically, the influence of conductive objects on the MI channel in complex environments is first investigated and then an environment-aware algorithm for the conductive objects is developed. Based on the environment-aware measurement obtained by the MI nodes, a joint device localization and conductive-object tomography algorithm is developed to estimate the position of the wireless devices as well as the distribution of conductive objects. In particular, the distribution of the conductive objects is quantized by the newly defined intensity magnitude. By adding the intensity magnitude as an input of the localization algorithm, the internode distances and orientations are determined and then the coordinates of nodes can be estimated. Finally, through numerical simulations and real-world experiments, the localization accuracy is analyzed and the environment-aware localization technique is validated to be better than that without the environment-aware capability.

The remainder of this paper is organized as follows. The related works are presented in Section II. The preliminaries, including the system architecture and the channel modeling of MI communications, are introduced in Section III. Then, we analyze the influence from the conductive objects in the complex environments to the MI channel in Section IV. In Section V, the localization algorithms based on the environment-aware result is presented. After that, we present the system implementation, experimental result and discussion in Section VI. Finally, this paper is concluded in Section VII.

II. RELATED WORK

The wireless sensor network becomes a solution for the localization in complex environments where the GPS does not work due to the lack of the line of sight to satellites. However, the localization for WSNs based on EM waves has problems when applied in the complex environments. In the wireless channel consisting of the RF-challenging propagation medium, such as underground and underwater, conventional wireless techniques based on the EM waves do not work due

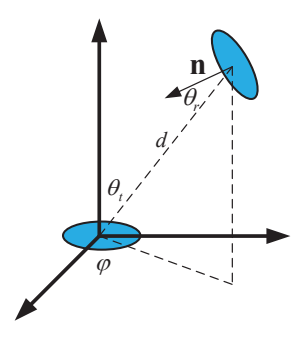


Fig. 1. MI technique based on two coupled coils

to the rapid attenuation of signal strength [9]. To address this problem, the wireless communication technique based on MI for RF-challenging environments is proposed in [25], after which many novel applications using MI-based communication are presented, including underground [26], underwater [24], pipelines [29], [30], and reserviors [27]. The availability of MI-based communication is demonstrated and evaluated by the experimental research in [28]. The preliminaries of the MI-based localization are provided by these research.

Another problem of traditional localization strategies is the requirement of pre-installed infrastructures. In the complex environments, anchors or RFID-tags are usually used to localize the mobile sensor nodes [5], [6], [7], [8], [19], [20], [21]. However, these strategies can be used in the known indoor environments but difficult to be applied in unknown or dynamic environments. Moreover, the localization error significantly increases as the distance from the anchors or tags increases due to the influence of the signal reflections. To address the problem caused by the signal reflections, fingerprint database for localization is built by aforehand training measurements to better relate the signal strength with the device position so that the localization performance can be improved [22], [23]. However, since these techniques require aforehand knowledge and numerous facilities, they are not easy to be applied in the unknown or dynamic environments.

Research on MI-based localization is developed in [31] and [32]. In [31], researchers propose methods for object localization using beacons of low frequency quasi-static magnetic field. To localize the object, the magnetometer readings on the object are processed to estimate the magnitude and phase of the received beacon signals. Due to the utilization of low frequency magnetic field, the signal can penetrate foliage, soil, buildings and has no direct influence by bad weather conditions and diurnal variations. In [32], the MI-based localization is utilized to solve the problem of RF-challenging environments. In this research, the magnetic induction and acoustic wireless communications are combined to localize the drag anchors in the seabed. The environments in these scenarios are considered as homogenous environments, which do not have any high-conductive objects to affect the magnetic field generated by the MI coils.

Although the MI signal has more stable and penetrable channel for the localization, it is still influenced by the high-conductive objects nearby. To apply the MI-based localization

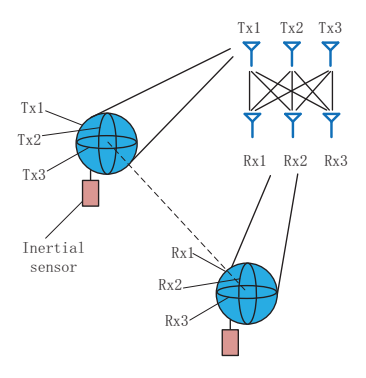


Fig. 2. 3-directional (3D) MI node.

in complex environments with conductive objects, the MI-based environment-aware localization is proposed for indoor environments in our previous work [1]. As a foundation of this paper, our previous work completes the channel modeling, the solution and the numerical analysis. As an extension, this paper considers the complex environments with arbitrary number of conductive objects, such as indoor, in-pipe, and underground environments. Then, we focus on the implementation of the localization techniques by developing an MI-based localization test-bed. The performance of the localization algorithm is evaluated by a series of in-lab experiments using the test-bed.

III. Preliminaries

A. System architecture

The 3-directional (3D) MI nodes shown in Fig. 2 are used to form the WSN for the environment-aware localization. The 3-directional (3D) MI sensor node is first designed to realize the omnidirectional coverage of the MI signal [27], which also provides the convenience to the MI-based localization. As shown in Fig. 2, three coils are wound orthogonally for a 3D MI node. Similar to a 3 × 3 MIMO system, the signal is delivered by the three transmitting coil Tx1, Tx2, Tx3 and received by the three receiving coils Rx1, Rx2 and Rx3. Therefore, totally 9 independent links are established between the transmitting node and the receiving node to provide more information input for the localization algorithm. Additionally, each MI node is equipped with an inertial sensor, which can sense the gravity and determine the orientation of the node.

Consider a network formed by a cluster of 3D MI sensor nodes as shown in Fig. 3. The objective of the localization technique is to determine the position of each node in the global coordinate system x - y - z. The localization algorithm can be concluded as three phases shown in Fig. 4. In the first phase, each MI node in this network uses its environment-aware capability to sense the distribution of conductive objects in the complex environment. The details of the environment-aware algorithm will be presented in Section V A. In the second phase, we try to establish communications between the MI nodes in this network. Based on the information obtained by the internode communications and the environment-aware capability, the relative positions of the communicating nodes, including the distance and directional angles, can be estimated.

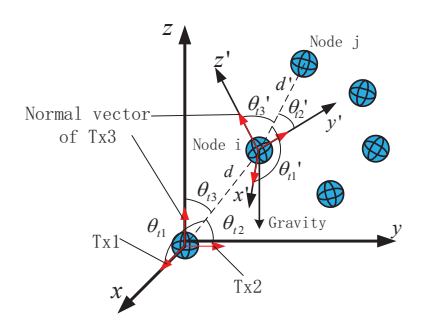


Fig. 3. The system architecture of the MI-based localization.

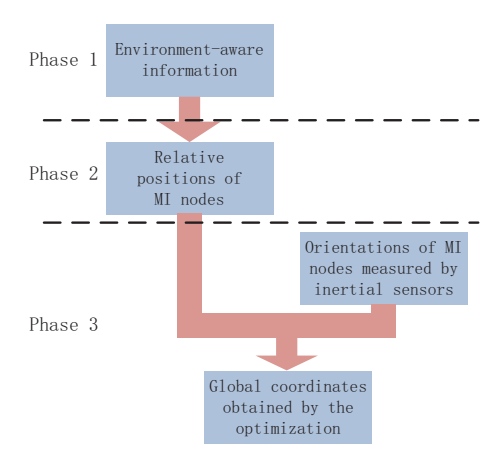


Fig. 4. The three-phase localization algorithm.

However, as shown in Fig. 3, once the relative positions of node i and node j determined by d', θ'_{t1} , θ'_{t2} , and θ'_{t3} are estimated, we can only find out the position of node j in the coordinate system x' - y' - z'. To determine the position in the global coordinate system x - y - z, additional work is need as the third phase. In the third phase, the inertial sensors equipped on MI nodes are used to determine the orientation of the node (the normal vector of Tx3). Based on the relative positions estimated in phase 2 and the orientations of nodes provided by the inertial sensors, we can formulate an optimization problem to determine the global position of each node. Details of phase 2 and phase 3 will be presented in Section V B.

B. Channel modeling in homogenous environments

Since MI techniques have good penetrating performance, most of materials are transparent to MI devices, except metal. Hence, the environments with less metallic objects can be considered as homogenous environments, which do not cause significant effect to MI signals.

The model of 3D MI channel has been developed in our previous work [30]. As shown in Fig. 1, the MI-based localization uses MI signals generated and received by two coupled coils. A small coil can be modeled as a magnetic dipole. Hence, the magnetic field generated by a coil is given by [33]:

$$\mathbf{H} \simeq \frac{NI_0 r^2}{4} \left(\mathbf{a}_r \frac{2}{d^3} cos\theta_t + \mathbf{a}_\theta \frac{1}{d^3} sin\theta_t \right) e^{-j\omega\left(t - \frac{d}{\delta}\right)} \tag{1}$$

Once another coil is deployed in the environment, the mutual induction between these two coils can be determined by taking the derivative of the magnetic flux with respect to the injected current [27]:

$$M \simeq \frac{d\phi}{dI_0} = \frac{d\left(\pi\mu r^2 \left| \mathbf{H} \cdot \mathbf{n} \right|\right)}{dI_0}$$
 (2)

where **n** is the normal vector of the receiving coil and μ is the permeability. Once the mutual induction is determined, the ratio of the received power to the transmitted power can be written as:

$$\frac{P_r}{P_t} \simeq \frac{\omega^2 M^2}{2R_0^2 + 2\omega^2 M^2} \tag{3}$$

where R_0 is the unit-length resistance of coil. ω is the operating frequency.

By substituting (2) into (3), the ratio of the received power to the transmitted power can be approximated as a function of distance d and intersection angles θ_r and θ_r :

$$\frac{P_r}{P_t} \simeq \frac{\mu^2 \omega^2 N^2 r^6}{\left(16R_0^2 + \mu^2 \omega^2 N^2\right) d^6} \cdot \left(\cos\theta_t \cos\theta_r - \frac{1}{2}\sin\theta_t \sin\theta_r\right)^2. \tag{4}$$

We can find from (4) that the received power is related to the intersection angles θ_t and θ_r shown in Fig. 1. For example, if $\theta_t = \frac{\pi}{2}$ and $\theta_r = 0$, two coils become orthogonal and the received power becomes zero. If θ_t , $\theta_r = 0$, two coils are facing each other and the received power can be maximized.

By considering the 3×3 channel obtained by the 3D MI nodes, the received power can be written as:

$$\mathbf{P_r} = \frac{k}{d^6} \cdot \mathbf{\Theta} \tag{5}$$

where P_r is a 3 \times 3 matrix of received power:

$$\mathbf{P_r} = \begin{bmatrix} P_{r1,1} & P_{r1,2} & P_{r1,3} \\ P_{r2,1} & P_{r2,2} & P_{r2,3} \\ P_{r3,1} & P_{r3,2} & P_{r3,3} \end{bmatrix}.$$
(6)

Here $P_{ri,j}$ indicates the received power in Rxj from transmitting coil Txi. The elements in Θ are related to the intersection angles between Txi and Rxj as shown in Fig. 5:

$$\Theta_{i,j} = \left(\cos\theta_{ti}\cos\theta_{rj} - \frac{1}{2}\sin\theta_{ti}\sin\theta_{rj}\right)^{2}.$$
 (7)

The coefficient k is related to the transmitting power and parameters of MI coils:

$$k = \frac{\mu^2 \omega^2 N^2 r^6 P_t}{16R_0^2 + \mu^2 \omega^2 N^2}.$$
 (8)

IV. Influence of Conductive Objectives on MI Systems

A complex environment for MI signals implies that many objects in this environment have high conductivity to significantly affect the MI signals. Many environments, such as indoor, underground, and in-pipeline environments can be considered as complex environments for the MI channel due to the existence of furniture, rebars, underground rocks, metallic pipewalls, and so on. To propose the MI-based localization for these complex environments, the analysis of the influence from these high-conductive objects is necessary.

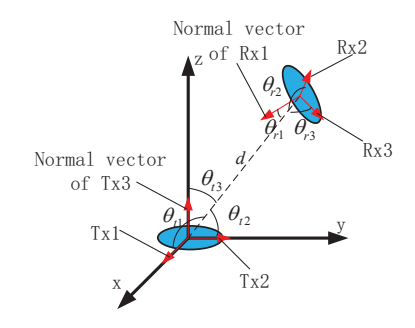


Fig. 5. Intersection angles of 3D MI nodes.

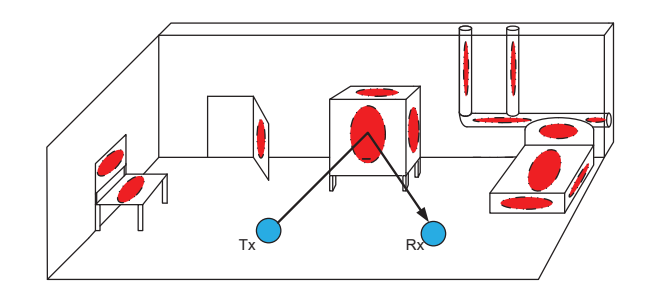


Fig. 6. The influence from the complex environment to MI signals.

An indoor environment with a lot of metallic furniture shown in Fig. 6 can be considered as a complex environment for the MI channel. In fact, no matter how complex the environment is, the objects in this environment can be considered as the combinations of conductive surfaces (the red area in the figure). Due to the eddy current induced on these surfaces, new magnetic field will be generated and the received signal becomes the superposition of the signals from the primary field and the new field generated by the eddy current. The influence from the conductive surfaces on MI signals can be analyzed as shown in Fig. 7. The magnetic field generated by the transmitting coil Tx induces the eddy current on a conductive surface. Based on the image theory, the magnetic field excited by this eddy current can be regarded as a signal generated by the image source Tx', which is symmetric to the original source Tx by the conductive surface. Therefore, the power from this new field can be written as:

$$P'_{r} \simeq \frac{C^{2} \mu^{2} \omega^{2} N^{2} r^{6} P_{t} cos^{2} \left(\frac{1}{2} \theta'\right)}{\left(16 R_{0}^{2} + \mu^{2} \omega^{2} N^{2}\right) d'^{6}}$$
(9)

where θ' and d' are the intersection angles and distance shown in Fig. 7. C is the reflection coefficient of magnetic field given by [27]:

$$C = \left| \frac{\mu_0 - \mu_1}{\mu_0 + \mu_1} \right| \tag{10}$$

where μ_0 and μ_1 are the effective permeability of the air and the conductive objects.

The power from a certain path can be calculated by the image method but the unknown parameters in this model make the calculation difficult. Fig. 8 shows three paths from the transmitter to the receiver in the complex environment with multiple conductive surfaces. The power from multi-paths

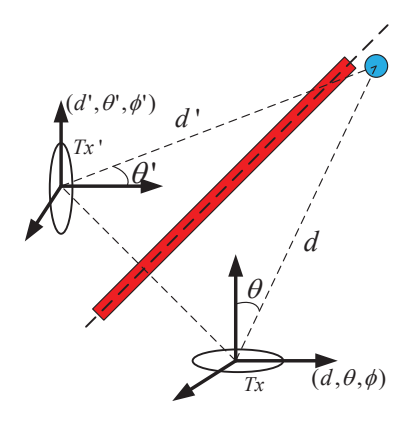


Fig. 7. The influence from the conductive surface to the MI signal.

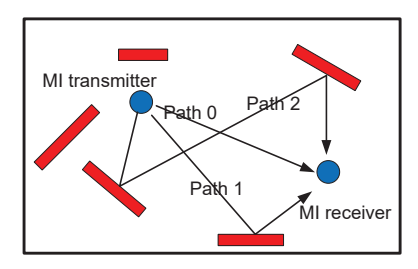


Fig. 8. The MI signal from multi-paths.

are different and dominated by the parameters according to (9). However, due to the uncertainties of the environment, the power from each path cannot be exactly calculated but analyzed by statistics.

When the signal from a path arrives at the receiving node, it has been affected by multiple conductive surfaces. After traveling a length of l and being affected by m conductive surfaces, the PDF of a path that intersects n conductive surfaces can be decomposed as [34]:

$$f(n, m|l) = f_1(n|l) \cdot f_2(m|n, l) \tag{11}$$

where $f_1(n|l)$ is the PDF for a path that has undergone n surfaces after traveling a distance of l. This function can be expressed as a Poisson distribution by the demonstration of Monte Carlo simulation:

$$f_1(n|l) = \frac{(\lambda l)^n}{n!} e^{-\lambda l} \tag{12}$$

where $\frac{1}{\lambda}$ is the mean free distance which is related to the dimension and deployment of conductive surfaces. The second function $f_2(m|n, l)$ gives the probability of having exactly m influencing surfaces on total n surfaces in the path length l:

$$f_2(m|n,l) = \binom{n}{m} p^m(l) q^{n-m}(l)$$
 (13)

where p, q are determined by:

$$p(l) = \frac{1 + e^{-\lambda(l-d)}}{2}, \quad q = 1 - p.$$
 (14)

Therefore, by considering the 3D MI nodes as transceivers, the power from a path with a length of l can be written as:

$$P(l) = \sum_{n=1}^{\infty} \sum_{m=1}^{n} f(n, m|l) \frac{C^{2m} \mu^2 \omega^2 N^2 r^6 P_t}{\left(16R_0^2 + \mu^2 \omega^2 N^2\right) l^6}$$
 (15)

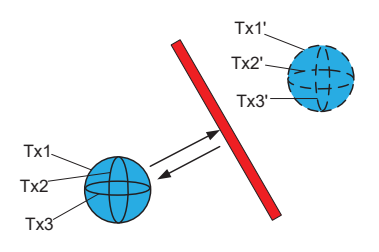


Fig. 9. Environmental awareness by MI node.

Intuitively, the power of MI signal decays with the increase of the number of influencing surfaces m and sixth order of the length l.

Since the MI-based communication utilizes the near field in HF band, the phase difference from different paths is negligible. Therefore, the total received power is simply defined as the summation of the power from individual paths regardless of the phase [34]:

$$P_{total}(d) \simeq P_r(d) + \sum_{i=1}^{\infty} P(d+i\sigma c)$$
 (16)

where c, σ are light speed and bin time unit, respectively. The bin time unit σ is determined by the bandwidth B that $\sigma = \frac{1}{B}$.

V. Localization algorithms

A. Environment-aware algorithms

Since usually the information of the environments is unknown to us, the mean free distance and reflection coefficients introduced in Section IV are not easy to be determined. Instead of knowing these parameters, the MI-based sensor nodes are used to sense the environment to determine the parameters. As shown in Fig. 9, we first use the MI coil Tx1 to transmit the signal with the power P_t . Due to the existence of the conductive surface nearby, the eddy current will be induced on the surface and the new magnetic field can be regarded as the signal generated by the image coil Tx1'. Therefore, the new field can be observed as the feedback by the coil Tx1, Tx2, and Tx3[35]. Similarly, Tx2 and Tx3 can transmit and receive the signal for environment-aware measurements. Therefore, totally 9 measurements can be measured:

$$\mathbf{P}_{\mathbf{r}i,i} = \begin{bmatrix} P_{r1,1}^* & P_{r1,2}^* & P_{r1,3}^* \\ P_{r2,1}^* & P_{r2,2}^* & P_{r2,3}^* \\ P_{r3,1}^* & P_{r3,2}^* & P_{r3,3}^* \end{bmatrix}.$$
(17)

where $P_{ri,j}^*$ is the received signal strength obtained by transmitting the signal from Txi and receiving in Txj.

The total received signal strength can be written as the 1-norm $\|\mathbf{P}_{\mathbf{r}i,i}\|_1$ and derived by substituting d = 0 into (16) and eliminate the direct-path term:

$$\|\mathbf{P}_{\mathbf{r}i,i}\|_{1} = P'_{total}(d=0) \simeq \sum_{i=1}^{\infty} P(i\sigma c)$$

$$= \sum_{i=1}^{\infty} \sum_{n=1}^{\infty} \sum_{m=1}^{n} f(n, m|i\sigma c) \frac{C^{2m} \mu^{2} \omega^{2} N^{2} r^{6} P_{t}}{\left(16R_{0}^{2} + \mu^{2} \omega^{2} N^{2}\right) (i\sigma c)^{6}}.$$
(18)

Denoting the intensity magnitude Λ as:

$$\Lambda = \sum_{i=1}^{\infty} \sum_{n=1}^{\infty} \sum_{m=1}^{n} \frac{f(n, m|i\sigma c) C^{2m}}{(i\sigma c)^{6}}$$
 (19)

(18) becomes:

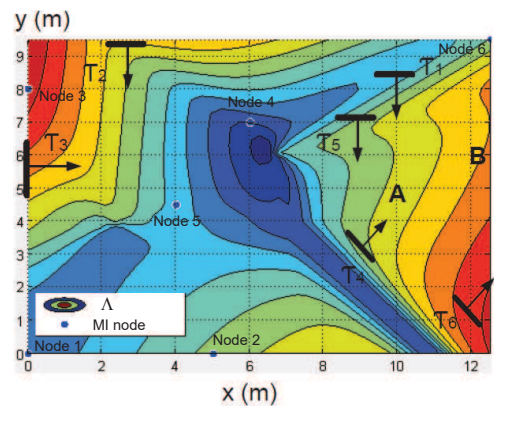
$$P'_{total}(d=0) \simeq \frac{\Lambda \mu^2 \omega^2 N^2 r^6 P_t}{16R_0^2 + \mu^2 \omega^2 N^2}.$$
 (20)

It is easy to learn from (19) that the intensity magnitude is related to the reflection coefficient, the number and density of objects nearby. Intuitively, the intensity magnitude increases if the node is deployed at more constricted environments with more conductive objects nearby. As a result, the developed intensity magnitude provides convenience to us to estimate the distribution of the conductive objects in the environment. Instead of estimating the reflection coefficient and mean free distance, estimating an entire function which includes those parameters becomes more applicable. According to (20), the intensity magnitude is estimated by:

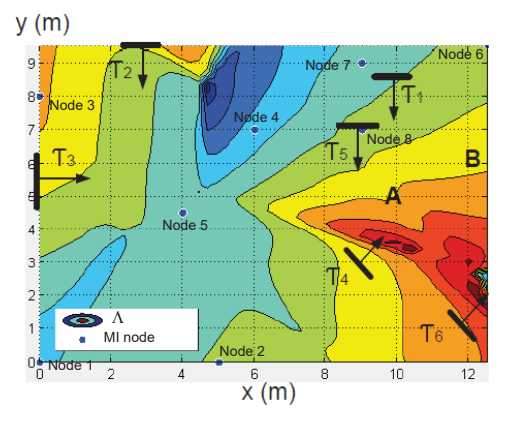
$$\hat{\Lambda} = \frac{P'_{total} \left(16R_0^2 + \mu^2 \omega^2 N^2 \right)}{\mu^2 \omega^2 N^2 r^6 P_t}.$$
 (21)

Consider an MI sensor network with multiple sensor nodes, each node can estimate the local intensity magnitude at its own position. Based on the intensity magnitude at different positions, a map of the intensity magnitude in this environment can be reconstructed by the biharmonic interpolation method.

An example of the environmental reconstruction is shown in Fig. 10. In this simulation, 3D MI nodes shown as the blue spots are deployed in an environment with multiple reflectors. The coils on the 3D MI nodes are simulated by 20 AWG wires with the unit-length resistance of $3.331 \times 10^{-2} \ \Omega/m$. All the coils have the same radius 15 cm and number of turns $N_c = 50$. An excited current with a frequency of 30 MHz is injected into the transmitting coil circuit. The black bars with arrows in Fig. 10 show the positions and directions of the conductive surfaces. To calculate the intensity magnitude on the nodes' positions, we consider that the signal generated by each coil will be affected once on each surface. In this case, the multihop paths are neglect since the signal becomes too weak to contribute the total received signal strength after going through multiple surfaces. As shown in Fig. 10(a), we first deploy 6 nodes to calculate the intensity magnitude. The colored map shows the reconstruction result by biharmonic interpolation. The area colored by red indicates the high intensity magnitude and it turns to blue with the intensity magnitude decreasing. Since the environmental reconstruction is obtained by the interpolation. The result will be more accurate if more nodes are deployed for the measurements. In Fig. 10(b), two more nodes (Node 7 and Node 8) are added and the result is different from it of Fig. 10(a). Obviously, the intensity magnitude at point A (marked in the map) should be higher than it at point B since point A is closer to the surfaces Γ_1 , Γ_4 and Γ_5 . However, due to the lack of measurements, the estimated potential at A is lower in Fig. 10(a). The accuracy of intensity magnitude at A and B is then improved in Fig. 10(b).



(a) The intensity magnitude sensed by 6 nodes.



(b) The intensity magnitude sensed by 8 nodes.

Fig. 10. The environmental reconstruction using intensity magnitude.

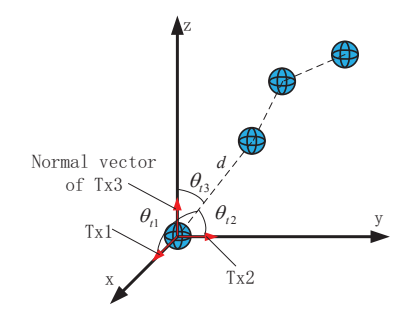
B. Estimation of nodes' positions

In this subsection, we propose the algorithm to determine the position of MI sensor nodes in the network. Consider a network with K MI nodes as shown in Fig. 11(a). We build the coordinate axis by locating the first node at the original point $\mathbf{p}_1 = (0,0,0)$. The normal vectors of Tx1, Tx2, Tx3 superpose the x, y, and z axis, respectively. Therefore, the coordinates of other nodes \mathbf{p}_2 , \mathbf{p}_3 , ..., \mathbf{p}_K in this network need to be determined in this coordinate system. According to the system architecture introduced in Section III A, communication links need to be established between these MI nodes. Intuitively, the localization accuracy will increase if more links are established to get more measurements.

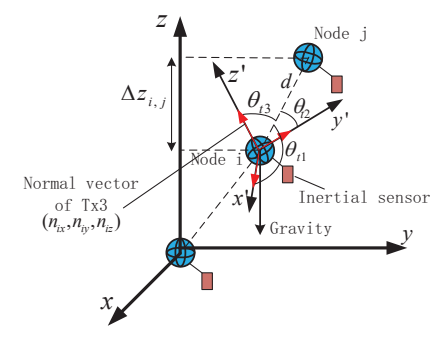
The RSSI measurements can be efficiently obtained by broadcasting. In the first time slot, we use Node 1 to broadcast and the other nodes keep hearing. Therefore, the K-1 measurements are obtained in total. Then, Node 2, Node 3, ..., and Node K broadcast successively so that a matrix of measurements can be obtained:

$$\mathbf{P_{m}} = \begin{bmatrix} \mathbf{P_{r1,1}} & \mathbf{P_{r1,2}} & \dots & \mathbf{P_{r1,K}} \\ \mathbf{P_{r2,1}} & \mathbf{P_{r2,2}} & \dots & \mathbf{P_{r2,K}} \\ \dots & \dots & \dots & \dots \\ \mathbf{P_{rK,1}} & \mathbf{P_{rK,2}} & \dots & \mathbf{P_{rK,K}} \end{bmatrix}.$$
(22)

where $\mathbf{P}_{\mathbf{r}i,j}$ $(i \neq j)$ is the measurement taken from the communication between Node i and Node j. Since each node has three transmitting/receiving coils, $\mathbf{P}_{\mathbf{r}i,j}$ is a 3 by 3 matrix



(a) The relative distance and directional angles.



(b) The relative position in the global coordinate system.

Fig. 11. Relative position of MI nodes in the network.

written as (6). The diagonal elements are the environment-aware measurements presented in (17).

Once a link is established between two MI nodes, the related position can be estimated based on the channel model of MI signals. We first consider the homogenous environments. Here all the coils have the same design and three transmitting coils have the same power P_t . According to (5), the inter-node distance d can be estimated by:

$$\hat{d} = \left(\frac{k}{\|\mathbf{P}_{\mathbf{r}}\|_1}\right)^{\frac{1}{6}}.\tag{23}$$

Then, the vector related to the intersection angles Φ is estimated by:

$$\hat{\mathbf{\Phi}} = \frac{d^6}{k} (\mathbf{P}_1 + \mathbf{P}_2 + \mathbf{P}_3) \tag{24}$$

where P_1 , P_2 and P_3 are column vectors by extracting each column from P_r :

$$\mathbf{P_r} = [\begin{array}{ccc} \mathbf{P_1} & \mathbf{P_2} & \mathbf{P_3} \end{array}]. \tag{25}$$

Φ is expressed as:

$$\mathbf{\Phi} = \begin{pmatrix} (\cos\theta_{t1} + \frac{1}{2}\sin\theta_{t1})^2 \\ (\cos\theta_{t2} + \frac{1}{2}\sin\theta_{t2})^2 \\ (\cos\theta_{t3} + \frac{1}{2}\sin\theta_{t3})^2 \end{pmatrix}. \tag{26}$$

Obviously, once the vector $\mathbf{\Phi}$ is estimated, the intersection angles θ_{t1} , θ_{t2} and θ_{t3} are determined. Therefore, the relative position of two MI nodes can be determined by \hat{d} and $\hat{\mathbf{\Phi}}$.

Then we estimate the related position by considering the complex environments. Since the internode distances are usually meter-level, we have $\sigma c \gg d$. Therefore, (16) can be approximated as:

$$P_{total}(d) \simeq P_r(d) + \sum_{i=1}^{\infty} P(d + i\sigma c) \approx P_r(d) + \sum_{i=1}^{\infty} P(i\sigma c)$$

$$\simeq \frac{\mu^2 \omega^2 N^2 r^6 P_t}{16R_0^2 + \mu^2 \omega^2 N^2} \left(\frac{1}{d^6} + \bar{\Lambda}\right)$$
(27)

where $\bar{\Lambda}$ is the intensity magnitude around the transmitting node and receiving node determined by $\bar{\Lambda} = \sqrt{\hat{\Lambda}_t \hat{\Lambda}_r}$. $\hat{\Lambda}_t$ and $\hat{\Lambda}_r$ are the intensity magnitudes estimated at transmitting node and receiving node, respectively. By considering the 3×3 link, the internode distance and intersection angles are estimated by:

$$\hat{d} = \left(\frac{\|\mathbf{P_r}\|_1}{k} - \bar{\Lambda}\right)^{-\frac{1}{6}} \tag{28}$$

$$\hat{\mathbf{\Phi}} = \frac{d^6}{k} \left(\mathbf{P_1} + \mathbf{P_2} + \mathbf{P_3} - k\bar{\mathbf{\Lambda}} \right) \tag{29}$$

where $\bar{\Lambda}$ is a column vector with elements $\bar{\Lambda}_i = \sqrt{\hat{\Lambda}_{ti}\hat{\Lambda}_r}$. $\hat{\Lambda}_{ti}$ is the estimated intensity magnitude by transmitting the signal from the *i*-th (i = 1, 2, 3) coil and capturing the feedback by the node itself. Therefore, the relative position of two nodes is estimated by considering the influence from the complex environments.

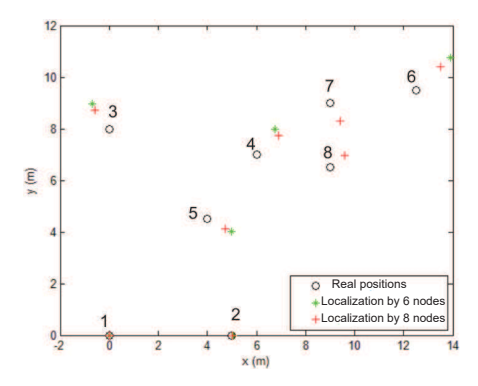
The coordinate of each node needs to be determined in the global coordinate system based on the relative positions and the nodes' orientations measured by inertial sensors. Since the proposed MI-based localization can estimate not only the internode distance but also the relative orientations, x-, y- and z-coordinates can be independently estimated by solving three optimization problems. We first discuss the estimation of z-coordinates. Based on the estimated \hat{d} , $\hat{\Phi}$, and the normal vector of Tx3 of node i (n_{ix}, n_{iy}, n_{iz}) measured by the inertial sensor, the difference of node i and node j on z-coordinates can be expressed as:

$$\Delta z_{i,j} = n_{iz} \hat{d}_{i,j} cos \hat{\theta}_{i,3} \tag{30}$$

The estimation of z-coordinates of nodes $(z_2, z_3, ..., z_K)$ in this network can be formulated as following minimization:

$$\min_{z_2, z_3, \dots, z_K} \sum_{(i, j) \in A} \left| (z_i - z_j)^2 - \Delta z_{i, j}^2 \right| \tag{31}$$

where A is called the neighbor set defined as $A := \{(i, j) : \|\mathbf{p}_i - \mathbf{p}_j\| \le R_c\}$. Here R_c is the communication range for the MI sensor nodes. $d_{i,j}$ and $\theta_{i,3}$ are respectively the measured internode distance and intersection angle shown in Fig. 11(a). Since (31) is nonconvex, it is necessary to convert it to a convex optimization problem for a global solution. Here we reformulate it by using relaxation method. As a first step, we rewrite (31) as:



(a) Estimated positions compared with real positions

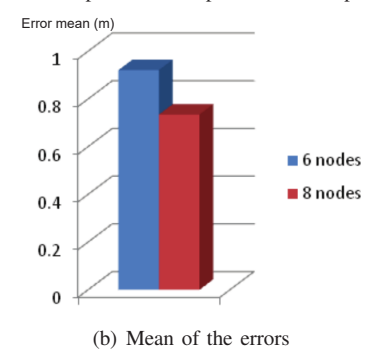


Fig. 12. A comparison between 6 nodes and 8 nodes.

Relaxing the equality constraints to "≥" yields the following convex problem [36]:

$$\min_{z_{2}, z_{3}, \dots, z_{K}, a_{i,j}} \sum_{(i,j) \in A} \left| a_{i,j} - \Delta z_{i,j}^{2} \right|$$

$$s.t. \quad a_{i,j} \ge (z_{i} - z_{j})^{2}, \quad \forall (i,j) \in A$$
(33)

which is a second-order cone programming (SOCP) for solving the original problem. Finally, we rewrite it to the standard form:

$$\min_{z_{2}, z_{3}, \dots, z_{K}, a_{i,j}, t_{i,j}} \sum_{(i,j) \in A} t_{i,j}
s.t. \quad a_{i,j} \ge (z_{i} - z_{j})^{2},
t_{i,j} \ge |a_{i,j} - \Delta z_{i,j}^{2}|, \quad \forall (i,j) \in A.$$
(34)

Therefore, the z-coordinates of the MI sensor nodes can be determined by solving above optimization problem. Similarly, the x-, y- coordinates can be estimated by respectively using $\theta_{i,1}$, $\theta_{i,2}$ instead of $\theta_{i,3}$, and using n_{ix} , n_{iy} instead of n_{iz} in above optimization problem.

Due to the approximation used in (27), errors will be caused when we estimate the relative position of each pair. The formulated optimization problem aims at minimizing the mean of the positioning errors by considering the measurements from all the communication pairs in this network. Intuitively, the mean of errors can be reduced if more nodes are deployed to establish more links for the measurements. The simulation in Fig. 12 shows the improvement of positioning accuracy when a network with more nodes and links is used. In this simulation, we use the same scenario and parameters as used in Fig. 10. Each node is assumed to communicate with all the other nodes in this network. The black circles indicate the real

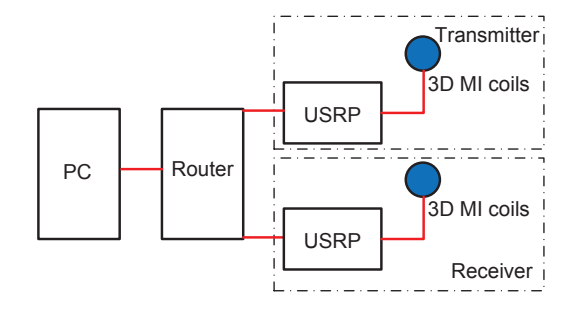


Fig. 13. Signal generation and observation.



Fig. 14. USRP N210.

positions of nodes. The estimated positions of the original 6 nodes are marked as green stars while the updated localization results of the 8 nodes are marked as red stars. The mean of positioning errors are calculated as shown in Fig. 12(b). The mean of errors is reduced by about 0.2 meters when 2 more nodes are added.

VI. EXPERIMENTAL IMPLEMENTATION AND RESULT

In this section, we test the developed MI-based localization algorithm by a series of in-lab experiments on the MI-based localization test-bed.

A. System design and experimental facilities

The architecture of MI-based localization test-bed can be developed as shown in Fig. 13. The signal generation and observation modules are formed by the USRPs with the control of PC. As shown in Fig. 14, USRP N210 is used that equipped with a Xilinx Spartan-3A DSP 3400 FPGA, a 100 MS/s dual ADC, a 400 MS/s dual DAC, and a gigabit ethernet connectivity to stream data to and from host PCs. Two 3D MI coils, performing as the antennas, are designed by enwinding the wires on the cubic frames shown in Fig. 15 with following parameters: The edge length of the cube $l_c = 10cm$. The number of turns for each coil N = 8. The conductivity of the wire $\sigma = 0.1339\Omega/m$ (26 AWG). According to the localization algorithm using a network introduced in V B, the orientation of each node is required to determine the nodes' positions in the global coordinate system. In this implementation, the 9DOF RAZOR IMU shown in Fig. 15 is used to measure the orientation of each node.

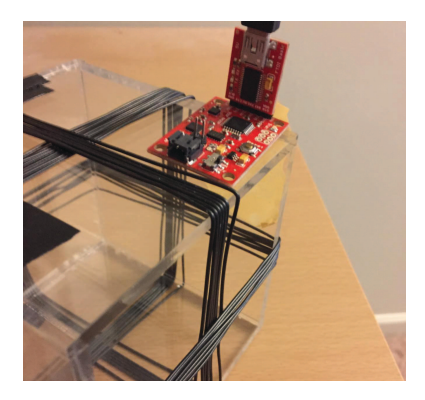


Fig. 15. The 3D MI node equipped with an inertial sensor.



Fig. 16. A view of MI-based localization (case 1).

B. Experimental result and discussion

As shown in Fig. 16 (case 1), we first test the localization algorithm on the floor of a lab. To compare the result of node-to-node localization and the localization by a network using the optimization presented in Section V B, we implement the localization in two ways shown in Fig. 17. In Fig. 17(a), the transmitting node is deployed at the original point (blue spot) as the anchor. The receiving node is deployed at the test positions (red spot) to be localized. Then, we deploy a network with 6 nodes as shown in Fig. 17(b). In this network, each pair of nodes can communicate so that 30 links are established (The transmitter and receiver can be interchanged). The position of the first node is known by (0,0) and the other 5 nodes need to be localized in the global coordinated system.

The experimental results are shown from Fig. 18 to Fig. 21.

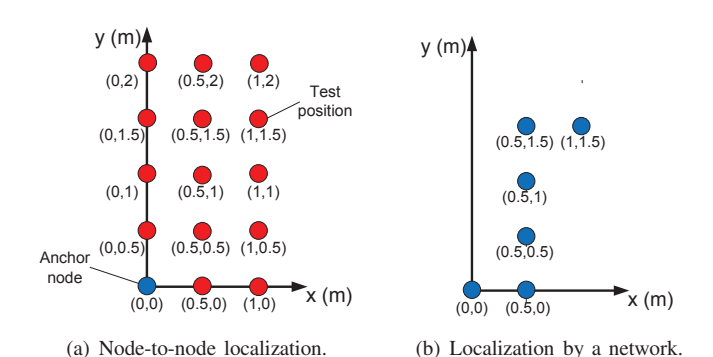


Fig. 17. The deployment of nodes in the experiment.

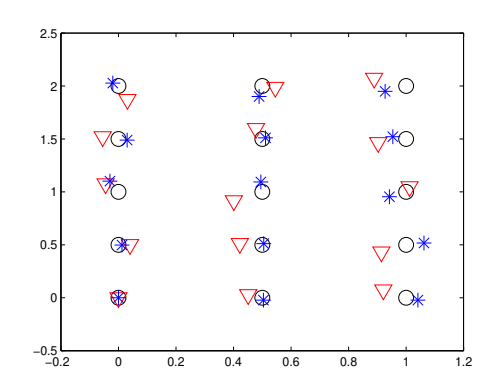


Fig. 18. Node-to-node localization (case 1).

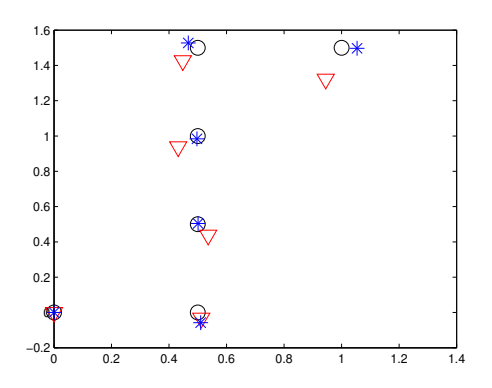


Fig. 19. Localization by a network (case 1).

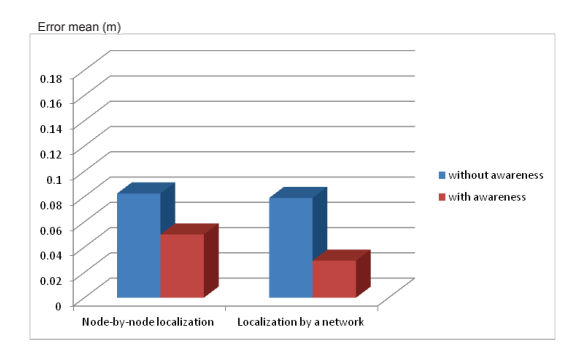


Fig. 20. Error mean (case 1).

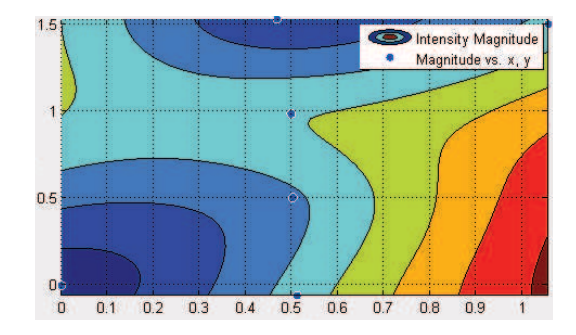


Fig. 21. Intensity magnitude (case 1).

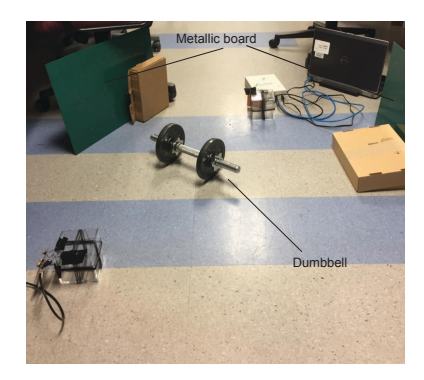


Fig. 22. A view of MI-based localization (case 2).

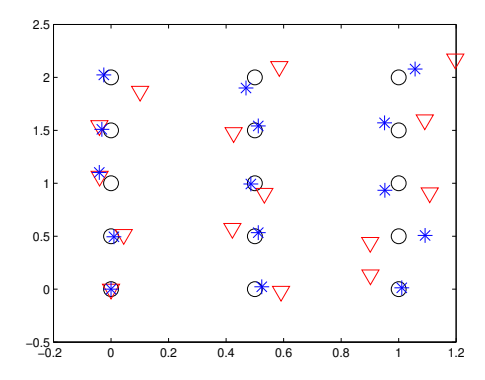


Fig. 23. Node-to-node localization (case 2).

The black circles in Fig. 18 and Fig. 34 indicate real positions of MI-based sensor nodes. The blue stars are the estimated positions obtained from the developed environment-aware localization algorithm. To compare with the environment-aware localization, the localization technique without environment-aware capability is implemented and the result is shown as the red triangles in the figures. In Fig. 20, the mean error of the localization is evaluated. Obviously, shown as the red bars, the localization is more accurate when the environment-aware capability is applied. In Fig. 26, after estimating the positions and the intensity magnitude of the 6 nodes, the reconstruction of the environment can be obtained by biharmonic interpolation. The intensity magnitude at the right side is higher than it at left side since the nodes are close to some metallic furniture on the right and the aisle exists on the left side of the map.

As shown in Fig. 22 (case 2), we implement the localization algorithm by deploying some metallic objects, such as metallic boards and a dumbbell. The same deployment scenarios shown in Fig. 17 are used. The localization result is shown from Fig. 23 to Fig. 25. Shown as the map in Fig. 26, the positions of two metallic boards and the dumbbell are estimated by environmental reconstructions since those high-conductive objects are easily detected due to the large influence to the MI signals.

From Fig. 27 to Fig. 31 (case 3), we test the environment-aware localization by deploying a pipeline-like structure. The same deployment scenario as case 1 and case 2 is used for the MI-based sensor nodes. The blue bars in Fig. 30 shows that the error becomes extremely large without considering

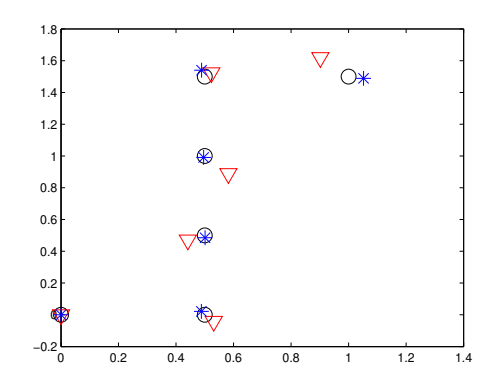


Fig. 24. Localization by a network (case 2).

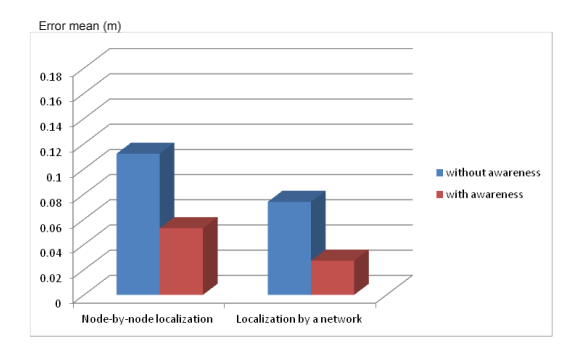


Fig. 25. Error mean (case 2).

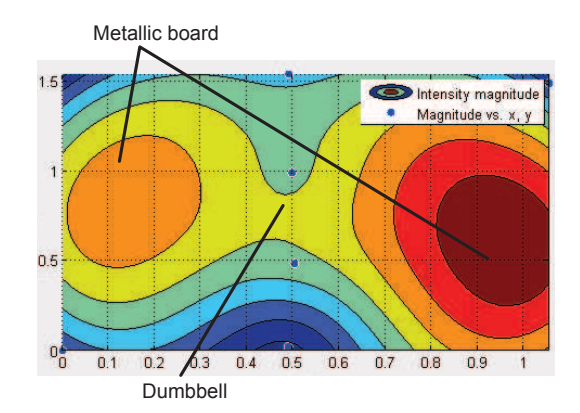


Fig. 26. Intensity magnitude (case 2).



Fig. 27. A view of MI-based localization (case 3).

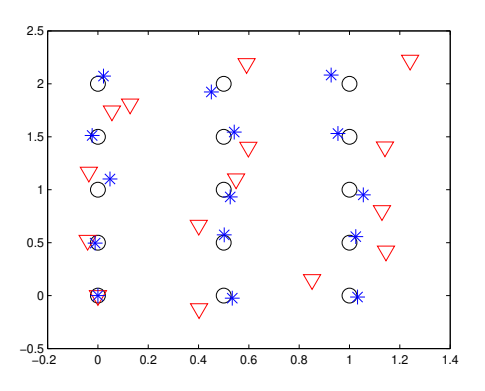


Fig. 28. Node-by-node localization (case 3).

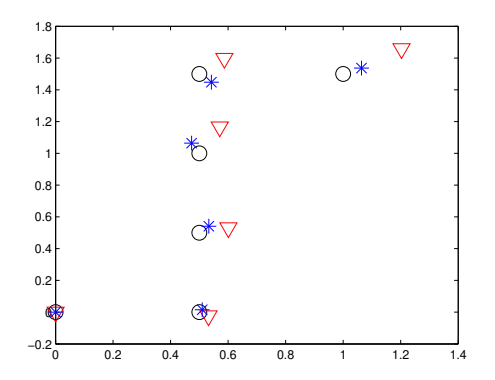


Fig. 29. Localization by a network (case 3).

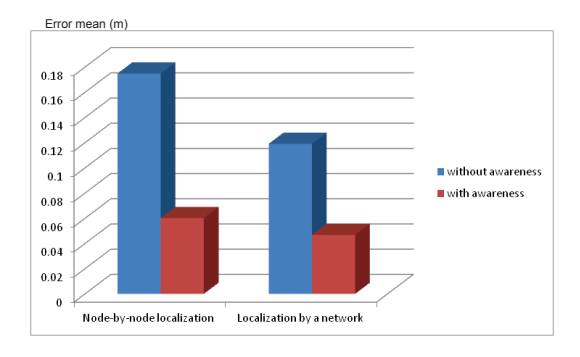


Fig. 30. Error mean (case 3).

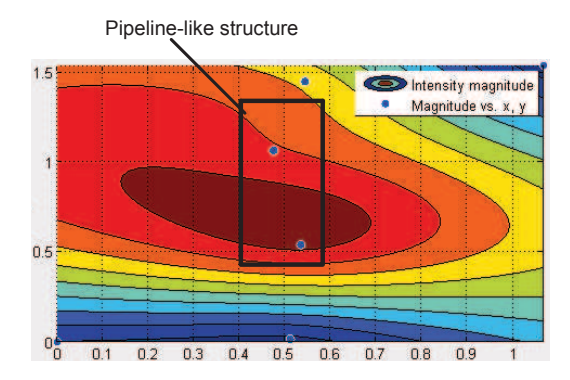


Fig. 31. Intensity magnitude (case 3).

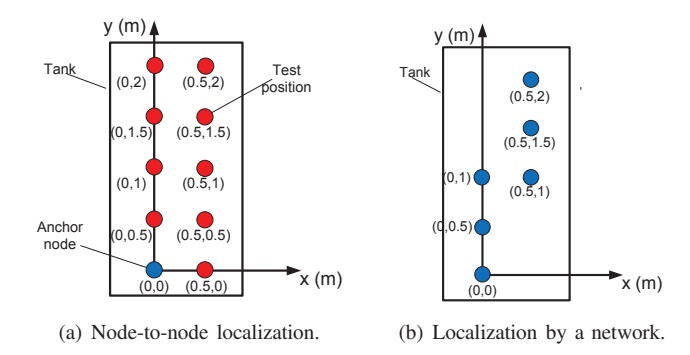


Fig. 32. The deployment of nodes for case 4 (in the tank).



Fig. 33. Simulated underground environment.

the influence from the environments, while the accuracy is significantly improved by the environment-aware capability of MI nodes shown as the red bars. The position of the pipeline-like structure is estimated by the red area in Fig. 31.

To test the localization algorithm in the RF-challenging environments, the MI-based sensor nodes are buried in the simulated underground environment shown in Fig. 33. In this implementation, an acrylic tank with a size of 255 cm \times 76 cm \times 76 cm (length \times width \times height) is set up on a pedestal. About 980000 cm^3 of sand is poured into the tank serving as the base material for the underground environment. Since usually the soil medium contains a certain concentration of water with electrolyte [28], which is the dominate factor that can influence the performance of underground communication,

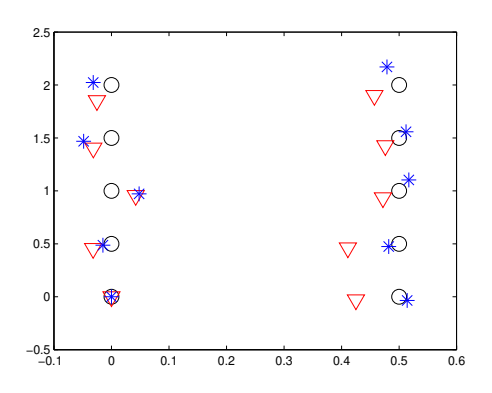


Fig. 34. Node-by-node localization (case 4).

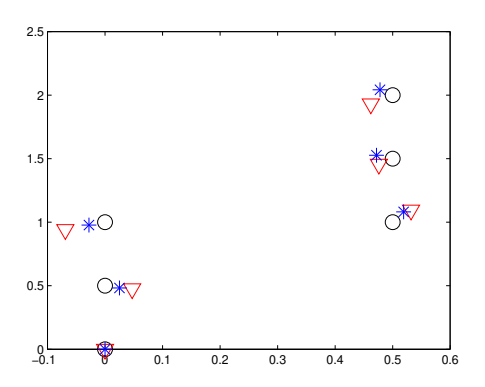


Fig. 35. Localization by a network (case 4).

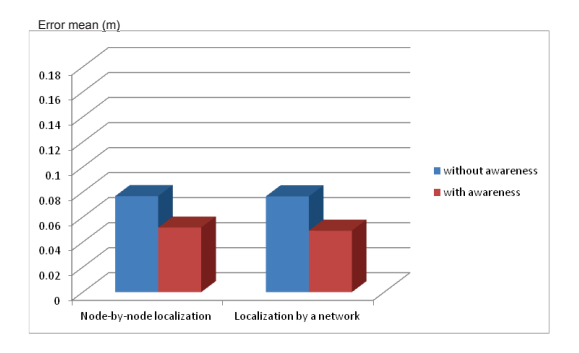


Fig. 36. Error mean (case 4).

a certain volume of of water is poured into the tank and mixed with the sand. Since the dimension of simulated underground environment is different from it of in-lab environment, the deployment of nodes is changed as shown in Fig. 32. Similarly, we did the node-to-node localization (Fig. 32(a)) and the localization by a network (Fig. 32(b)). The localization result is shown from Fig. 34 to Fig. 36. In the reconstruction map shown in Fig. 37, the right side turns to red since the tank is placed against the wall with metallic structures inside. The calculated intensity magnitude becomes much higher than it at the left side.

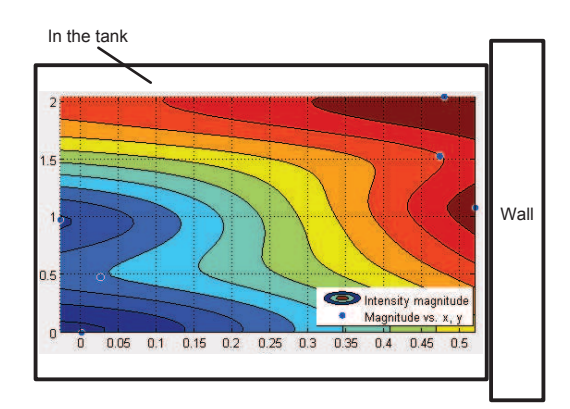


Fig. 37. Intensity magnitude (case 4).

VII. Conclusion

In this paper, an environment-aware localization algorithm is developed for MI-based wireless sensor networks. Different from existing MI localization solutions that only work in ideal and homogeneous environments, the developed algorithm can handle real-world complex environments with arbitrary number of conductive objects. In particular, each MI sensor node can be used as a "radar" to capture the influence of the surrounding environment on the MI channel. Then by analyzing the measurements from each node in the network, the intensity magnitude of the environmental influence can be estimated. Finally, based on the estimated intensity magnitude and the cooperation among all MI nodes in the network, a joint node localization and conductive-object tomography algorithm is developed to estimate the position of the wireless devices as well as the distribution of conductive objects. Compared with the existing MI-based localization techniques, the experiment results show that the proposed environment-aware solution achieves significantly better localization accuracy, (i.e., average localization error of each node in the network is 61.7% less).

REFERENCES

- X. Tan and Z. Sun, "Environment-Aware Indoor Localization Using Magnetic Induction," 2015 IEEE Global Communication Conference (GLOBECOM), pp. 1-6, December, 2015.
- [2] N. A. Jones and S. V. Hum, "An Ultra-Wideband Spatial Filter for Time-of-Arrival Localization in Tunnels," *IEEE Transactions on Antennas and Propagation*, vol. 61, No. 10, pp. 5237-5248, July, 2013.
- [3] A. Markham, N. Trigoni, D. W. Macdonald and S. A. Ellwood, "Underground Localization in 3-D Using Magneto-Inductive Tracking," *IEEE Sensors Journal*, vol. 12, No. 6, pp. 1809-1816, December, 2011.
- [4] R. Diamant and L. Lampe, "Underwater Localization with Time-Synchronization and Propagation Speed Uncertainties," *IEEE Transac*tions on Mobile Computing, vol. 12, No. 7, pp. 1257-1269, April, 2012.
- [5] L. Cheng, C. Wu and Y. Zhang, "Indoor Robot Localization Based on Wireless Sensor Networks," *IEEE Transactions on Consumer Electronics*, vol. 57, No. 3, pp. 1099-1104, August, 2011.
- [6] B. Wang, S. Zhou, W. Liu and Y. Mo, "Indoor Localization Based on Curve Fitting and Location Search Using Received Signal Strength," *IEEE Transactions on Industrial Electronics*, vol. 62, No. 1, pp. 572-582, June, 2014
- [7] A. Maddumabandara, H. Leung and M. Liu, "Experimental Evaluation of Indoor Localization Using Wireless Sensor Networks," *IEEE Sensors Journal*, vol. 15, No. 9, pp. 5288-5237, June, 2015.
- [8] Y. Tian, Z. Tang and Y. Yu, "Third-Order Channel Propagation Model-Based Indoor Adaptive Localization Algorithm for Wireless Sensor Networks," *IEEE Antennas and Wireless Propagation Letters*, vol. 12, pp. 1578-1581, December, 2013.
- [9] D. Wu, D. Chatzigeorgiou, K. Y. Toumi and R. B. Mansour, "Node Localization in Robotic Sensor Networks for Pipeline Inspection," *IEEE Transactions on Industrial Informatics*, vol. 12, No. 2, pp. 809-819, August, 2015.
- [10] G. Han, C. Zhang, L. Shu and J. Rodrigues, "Impacts of Deployment Strategies on Localization Performance in Underwater Acoustic Sensor Networks," *IEEE Transactions on Industrial Electronics*, vol. 62, No. 3, pp. 1725-1733, October, 2014.
- [11] R. Kaune, "Accuracy Studies for TDOA and TOA Localization," 15th International Conference on Information Fusion, pp. 408-415, July, 2012.
- [12] J. Xu, M. Ma and C. L. Law, "AOA Cooperative Position Localization," Global Telecommunications Conference, pp. 1-5, November, 2008.
- [13] Q. Luo, Y. Peng, J. Li and X. Peng, "RSSI-Based Localization Through Uncertain Data Mapping for Wireless Sensor Networks," *IEEE Sensors Journal*, vol. 16, No. 9, pp. 3155-3162, February, 2016.
- [14] F. Yaghoubi, A. A. Abbasfar and B. Maham, "Energy-Efficient RSSI-Based Localization for Wireless Sensor Networks," *IEEE Communications Letters*, vol. 18, No. 6, pp. 973-976, April, 2014.

- [15] P. Pivato, L. Palopoli and D. Petri, "Accuracy of RSS-Based Centroid Localization Algorithms in an Indoor Environment," *IEEE Instrumenta*tion and Measurement, vol. 60, No. 10, pp. 3451-3460, May, 2011.
- [16] R. Kaune, "Accuracy Studies for TDOA and TOA Localization," 15th International Conference Information Fusion (FUSION), pp. 408-415, July, 2012.
- [17] Jun Xu, Maode Ma and Choi Look Law, "AOA Cooperative Position Localization," Global Telecommunications Conference (GLOBECOM), November, 2008.
- [18] I. F. Akyildiz and E. P. Stuntebeck, "Wireless underground sensor networks: Research challenges," Ad Hoc Networks (Elsevier) Journal, vol.4, issue 6, November, 2006.
- [19] J. H. Kim, G. Sharma, N. Boudriga and S. S. Iyengar, "SPAMMS: A sensor-based pipeline autonomous monitoring and maintenance system," 2010 Second International Conference on Communication Systems and Networks (COMSNETS), January, 2010.
- [20] Y. L. Lai and J. Cheng, "A Cloud-Storage RFID Location Tracking System," *IEEE Transactions on Magnetics*, vol. 50, No. 7, July, 2014.
- [21] P. Yang, W. Wu, M. Moniri and C. C. Chibelushi, "Efficient Object Localization Using Sparsely Distributed Passice RFID Tags," *IEEE Transactions on Industrial Electronics*, vol. 60, No. 12, pp. 5914-5924, November, 2012.
- [22] S. Soonjun, D. Boontri and P. Cherntanomwong, "A Novel Approach of RFID Based Indoor Localization Using Fingerprinting Techniques," 15th Asia-Pacific Conference on communications, pp. 475-478, October, 2009.
- [23] Q. D. Vo and P. De, "A Survey of Fingerprint-Based Outdoor Localization," *IEEE Communications Surveys and Tutorials*, vol. 18, No. 1, pp. 491-506, June, 2015.
- [24] I. F. Akyildiz, P. Wang and Z. Sun, "Realizing Underwater Communication through Magnetic Induction," *IEEE Communication Magazine*, vol. 53, No. 11, pp. 42-48, November, 2015.
- [25] Z. Sun and I. F. Akyildiz, "Magnetic Induction Communications for Wireless Underground Sensor Networks," *IEEE Transactions on Antennas* and Propagation, vol.58, No. 7, pp. 2426-2435, July, 2010.
- [26] Z. Sun and I. F. Akyildiz, "On capacity of magnetic induction-based wireless underground sensor networks," *IEEE 2012 INFOCOM*, pp. 370-378, March, 2012.
- [27] H. Guo and Z. Sun, "Channel and Energy Modeling for Self-Contained Wireless Sensor Networks in Oil Reservoirs," *IEEE Transactions on Wireless Communications*, Vol. 13, No. 4, pp. 2258-2269, March, 2014.
- [28] X. Tan, Z. Sun and I. F. Akyildiz, "A Testbed of Magnetic Induction-based Communication System for Underground Applications," *IEEE Antennas and Propagation Magazine*, Vol. 57, No. 4, pp. 74-87, August, 2015
- [29] Z. Sun, P. Wang, M. C. Vuran, M. A. AI-Rodhaan, A. M. AI-Dhelaan and I. F. Akyidiz, "MISE-PIPE:Magnetic induction-based wireless sensor networks for underground pipeline monitoring," *Ad Hoc Networks*, vol.9, May, 2011.
- [30] X. Tan, Z. Sun and P. Wang, "On Localization for Magnetic Induction-based Wireless Sensor Networks in Pipeline Environments," 2015 IEEE International Conference on Communications (ICC), pp. 2780-2785, June, 2015.
- [31] A. Sheinker, B. Ginzburg, N. Salomonski, L. Frumkis and B. Z. Kaplan, "Localization in 2D Using Beacons of Low Frequency Magnetic Field," *IEEE Journal of Selected Topics in Applied Earth Obsercations and Remote Sensing*, vol. 6, No. 2, pp. 1020-1030, September, 2012.
- [32] S. S. Ge, Z. Zhao, W. He and Y. S. Choo, "Localization of Drag Anchor in Mooring Systems Via Magnetic Induction and Acoustic Wireless Communication Network," *IEEE Journal of Oceanic Engineering*, vol. 39, No. 3, pp. 515-525, September, 2013.
- [33] D. R. Frankl, Antenna Theory, Prentice Hall, 2005.
- [34] M. H. Ali and K. Pahlavan, "A New Statistical Model for Site-Specific Indoor Radio Propagation Prediction Based on Geometric Optics and Geometric Probability," *IEEE Transactions on Wireless Communications*, vol. 1, No. 1, pp. 112-124, January, 2002.
- [35] Y. Das, "Effects of Soil Electromagnetic Properties on Metal Detectors," IEEE Transactions on Geoscience and Remote Sensing, vol. 44, No. 6, pp. 1444-1453, June, 2006.
- [36] S. Srirangarajan, A. H. Tewfik and Z. Q. Luo, "Distributed sensor network localization using SOCP relaxation," *IEEE Transactions on Wireless Communications*, vol. 7, No. 12, pp. 4886-4895, December, 2008.